Chem

Article

Reducing polysulfide hydrodynamic radius toward low-temperature lithium–sulfur batteries

Graphical abstract

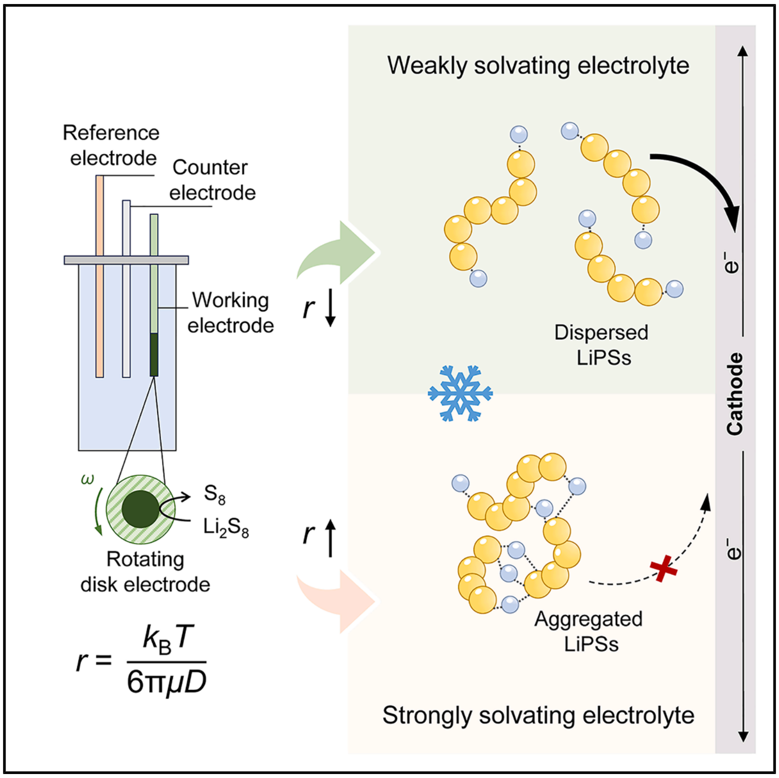

Highlights

- Establishing analytic methodology for quantifying intrinsic polysulfide kinetics
- Revealing reduced polysulfide hydrodynamic radius in weakly solvating electrolytes
- Validating low-temperature Li-S battery performance of weakly solvating electrolyte

Authors

Tian Jin, Meng Zhao, Xi-Yao Li,
Zi-Xian Chen, Bo-Quan Li, Jia-Qi Huang,
Qiang Zhang

Correspondence

zhao-meng@mail.tsinghua.edu.cn (M.Z.),
zhang-qiang@mails.tsinghua.edu.cn
(Q.Z.)

In brief

Rotating disk electrode analysis is conducted to quantify the lithium polysulfide reaction kinetics and reveals that the hydrodynamic radius of lithium polysulfides decreases as the electrolyte solvating power reduces, corresponding to inhibited lithium polysulfide aggregation. Unexpected low-temperature performance advantages are achieved in working lithium-sulfur batteries using weakly solvating electrolytes.

Jin et al., 2026, Chem *12*, 102881
March 12, 2026
https://doi.org/10.1016/j.chempr.2025.102881

CellPress

Please cite this article in press as: Jin et al., Reducing polysulfide hydrodynamic radius toward low-temperature lithium–sulfur batteries, Chem (2025), https://doi.org/10.1016/j.chempr.2025.102881

Chem

CellPress

Article

Reducing polysulfide hydrodynamic radius toward low-temperature lithium–sulfur batteries

Tian Jin,[1,2] Meng Zhao,[3,*] Xi-Yao Li,[3] Zi-Xian Chen,[1,2] Bo-Quan Li,[1,2] Jia-Qi Huang,[1,2] and Qiang Zhang[3,4,5,6,*]

[1]School of Materials Science and Engineering, Beijing Institute of Technology, Beijing 100081, China

[2]School of Interdisciplinary Science, Beijing Institute of Technology, Beijing 100081, China

[3]Beijing Key Laboratory of Complex Solid State Batteries & Tsinghua Center for Green Chemical Engineering Electrification, Department of Chemical Engineering, Tsinghua University, Beijing 100084, China

[4]State Key Laboratory of Chemical Engineering and Low-Carbon Technology, Tsinghua University, Beijing 100084, China

[5]AI Solid State Battery Innovation Center, Yibin 644002, China

[6]Lead contact

*Correspondence: zhao-meng@mail.tsinghua.edu.cn (M.Z.), zhang-qiang@mails.tsinghua.edu.cn (Q.Z.)

https://doi.org/10.1016/j.chempr.2025.102881

THE BIGGER PICTURE Lithium-sulfur (Li-S) batteries hold great promise in realizing high energy density beyond 500 Wh kg^{-1}, yet they are critically hampered by the polysulfide shuttle effect. Weakly solvating electrolytes (WSEs) emerge as an essential strategy to fundamentally suppress shuttle-induced anode degradation and improve the battery cycling lifespan. However, the inherent reduction of lithium polysulfide (LiPS) reactivity in WSEs leads to sluggish cathodic kinetics, creating a pivotal performance bottleneck. Compounded by empirical electrolyte screening and the absence of quantitative tools to evaluate the intrinsic LiPS kinetics, this bottleneck severely hinders progress. Establishing a quantitative analytic framework to probe the intrinsic LiPS conversion kinetics in WSEs is therefore both a scientific imperative to decode the performance decay mechanisms and an urgent necessity to accelerate Li-S battery technology commercialization.

SUMMARY

Lithium–sulfur (Li–S) batteries are promising in realizing high energy density. Employing weakly solvating electrolytes (WSEs) further improves the anode stability. However, the lithium polysulfide (LiPS) redox kinetics is hindered in WSEs, and the underlying mechanism remains unclear. Herein, the LiPS kinetics in WSEs is quantitatively deciphered using rotating disk electrode analysis. The electron transfer number during oxidation is reduced in WSEs, evidencing intrinsically suppressed oxidation extent. Meanwhile, the diffusion coefficient and the electrolyte viscosity concurrently increase, implying a reduced LiPS hydrodynamic radius in WSEs based on the Stokes–Einstein relation and corresponding to inhibited LiPS molecular aggregation. Attributed to the reduced aggregation, WSE-based Li–S batteries exhibit record-low-temperature performances, delivering 8.0 mAh cm^{-2} and 303 Wh kg^{-1} at 0°C in 6 Ah-level pouch cells. This work establishes a new kinetic analysis methodology to guide rational electrolyte design and highlights the promise of WSEs to enable low-temperature Li–S batteries.

INTRODUCTION

Lithium–sulfur (Li–S) batteries represent pivotal next-generation energy storage systems, driven by their exceptional theoretical energy density of 2,600 Wh kg^{-1}.[1–3] The sulfur cathode undergoes complex multi-electron and multi-phase reactions involving the dissolution of sulfur, the generation of soluble lithium polysulfides (LiPSs), and the deposition of lithium sulfide during discharge and reversible processes during charge.[4–6] By promoting the LiPS kinetics using catalysts or redox mediators, Li–S pouch cells have rendered an actual energy density of 695 Wh kg^{-1}.[7]

Nevertheless, the dissolved LiPSs diffuse to the anodic compartment under a concentration gradient and react parasitically with lithium metal to render rapid anode failure and limited battery cycling lifespan.[8–10] Employing weakly solvating electrolytes (WSEs) can effectively mitigate the parasitic reactions and improve the anode stability by reducing the LiPS reactivity.[11,12] Typical WSEs incorporate solvents with weakly solvating power of LiPSs into routine ether-based electrolyte. For instance, the di-isopropyl sulfide co-solvent reduces the shuttle current by 86%, and the corresponding WSE realizes over 100 cycles in Ah-level pouch cells.[13] Similar WSEs using hexyl methyl ether

Please cite this article in press as: Jin et al., Reducing polysulfide hydrodynamic radius toward low-temperature lithium–sulfur batteries, Chem (2025), https://doi.org/10.1016/j.chempr.2025.102881

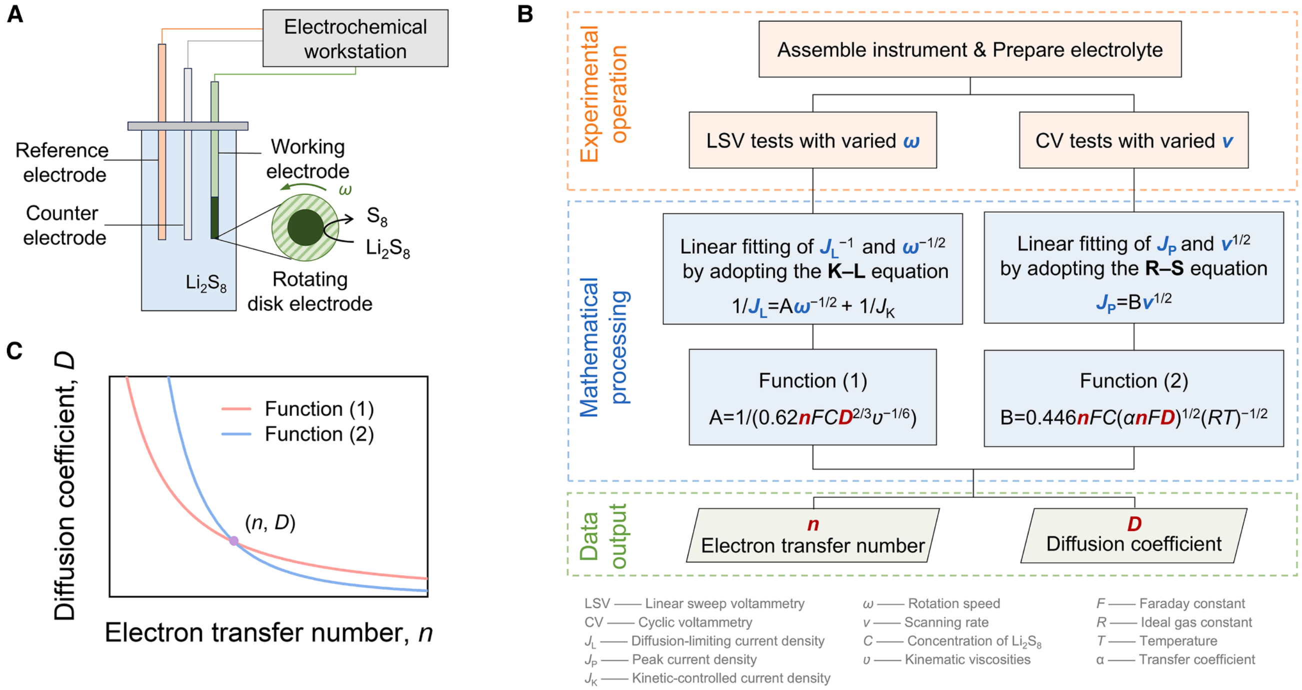

Figure 1. The RDE-based kinetic analysis methodology

(A) A three-electrode-based RDE configuration diagram.

(B) A workflow for evaluating the LiPS kinetic parameters.

(C) Schematic diagram of determining *n* and *D*.

(HME),[14] toluene,[15] or methyl propyl ether[16] all demonstrate improvement in anode stability and battery cycling lifespan.

Despite the advantages in promoting anode stability, the reduced LiPS reactivity in WSEs inevitably compromises cathodic reaction kinetics.[17] For instance, Li et al. demonstrated reduced discharge capacity as the electrolyte solvating power decreased.[18] Further polarization analysis identified the cathode activation polarization as the primary kinetic bottleneck in these systems.[19] Overcoming the dilemma of anode stability and cathode kinetics necessitates a deeper understanding of the LiPS kinetics in WSEs.

In this communication, the intrinsic LiPS kinetics in WSEs is quantitatively evaluated via rotating disk electrode (RDE) analysis. The electron transfer number (*n*) during LiPS oxidation reduces by 34.5% as the content of the weakly solvating solvent HME increases from 0% to 50%, manifesting the suppressed LiPS oxidation extent in WSEs. Concurrently, increasing HME content elevates the electrolyte viscosity while unexpectedly enhancing the LiPS diffusion coefficient (*D*). Based on the Stokes-Einstein relation, this counterintuitive *D* increase corresponds to a 65.8% reduction in the LiPS hydrodynamic radius, indicating significant inhibition of LiPS aggregation in WSEs. Leveraging these insights, Li–S batteries with WSEs exhibit exceptional low-temperature performances. A specific discharge capacity of 853 mAh g^{-1} is achieved at −20°C in WSEs and is 3.5 times promoted. Moreover, 6 Ah-level pouch cells with 8.2 mg_S cm^{-2} high-loading cathodes deliver a high areal capacity of 8.0 mAh cm^{-2} and an actual energy density of 303 Wh kg^{-1} at 0°C, significantly surpassing the currently reported low-temperature Li–S batteries.

RESULTS AND DISCUSSION

Reduced electron transfer but enhanced diffusion in WSEs

To quantify the intrinsic LiPS kinetic parameters in WSEs, an RDE analysis is proposed using three-electrode systems (Figure 1A). The RDE serves as the working electrode,[20] a Ag/AgCl electrode serves as the reference electrode, a lithium foil serves as the counter electrode, and WSEs containing Li_2S_8 with 0%, 10%, 20%, 30%, 40%, or 50% HME serve as the working electrolyte (Figures S1 and S2). The electrolyte physical properties, including density, dynamic viscosity (μ), and kinematic viscosity (υ), were measured in advance (Figures S3–S6). The intrinsic LiPS kinetic parameters of *n* and *D* are acquired using variable-rotation-speed linear sweep voltammetry (LSV) and variable-scan-rate cyclic voltammetry (CV) methods (Figure 1B). The LSV results are analyzed based on the Koutecký–Levich (K–L) equation,[21] and the diffusion-limiting current density (J_L) and the rotation speed (ω) are ruled by the following relation:

$$J_L^{-1} = A\omega^{-1/2} + J_K^{-1} \qquad \text{(Equation 1)}$$

Therein, J_K is the kinetic-controlled current density, and A is the slope of J_L^{-1} versus $\omega^{-1/2}$ and can be solved in the

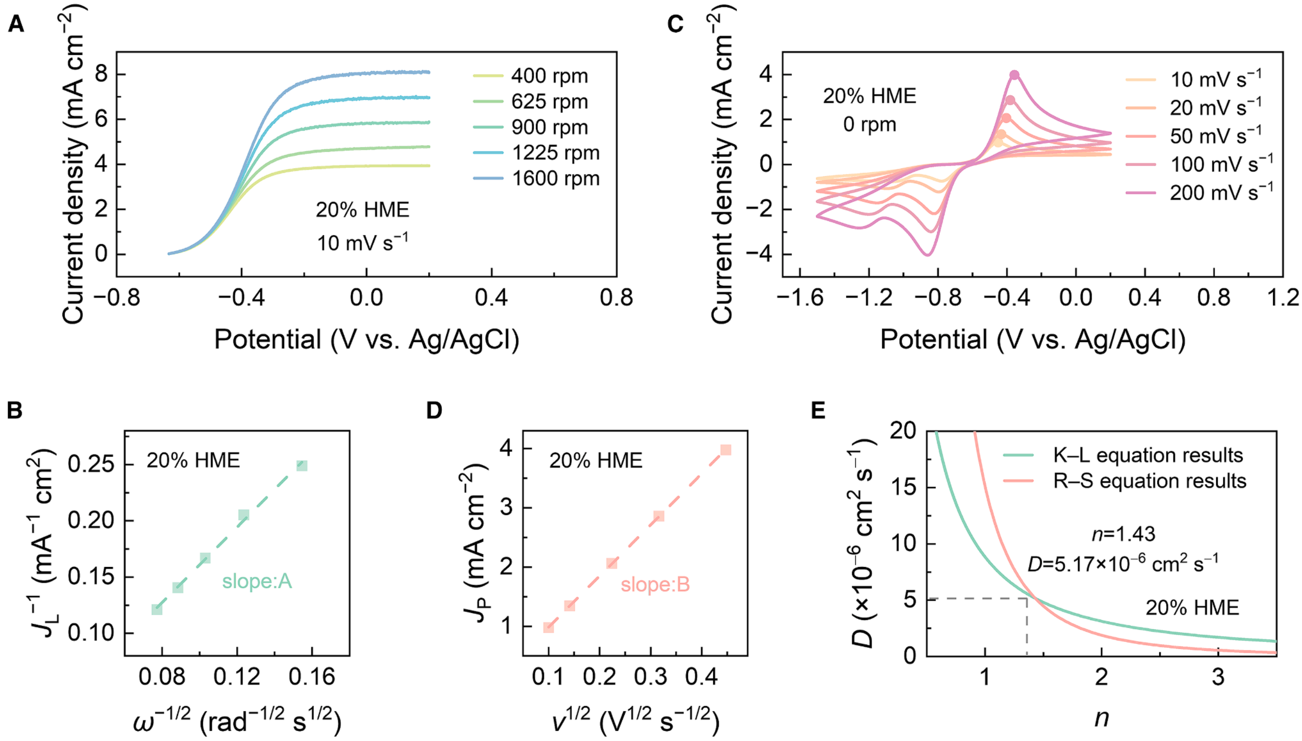

Figure 2. Determining the *n* and *D* values in 20% HME

(A and B) (A) Variable-rotation-speed LSV tests and (B) the corresponding fitted K–L plot.

(C and D) (C) Variable-scan-rate CV tests and (D) the corresponding fitted R–S plot.

(E) Combining K–L and R–S equations to solve the *n* and *D* values.

corresponding semi-infinite and forced-convection flow field as follows:

$$A = \left(0.62nFCD^{2/3}\upsilon^{-1/6}\right)^{-1} \qquad \text{(Equation 2)}$$

where F is the Faraday constant (96,485 C mol^{-1}), and C is the concentration of Li_2S_8.

The CV results are analyzed based on the Randles–Sevcik (R–S) equation,[22] and the peak current density (J_P) obeys the relationship with the scan rate (v) as follows:

$$J_P = Bv^{1/2} \qquad \text{(Equation 3)}$$

where B is the slope of J_P versus $v^{1/2}$ and can be solved as follows:

$$B = 0.446nFC(\alpha nFD)^{1/2}(RT)^{-1/2} \qquad \text{(Equation 4)}$$

Therein, α is the transfer coefficient (assumed to be 0.5 for reversible reactions), R is the ideal gas constant (8.314 J mol^{-1} K^{-1}), and T is the temperature. Based on Equations 2 and 4, the relation between n and D can be established, and the intersection of the two functions determines the n and D values (Figure 1C).

Following the above analysis methodology, we take the WSE with 20% HME as an example to solve for n and D. For the LSV tests, the rotating rate was controlled as 400, 625, 900, 1,225, or 1,600 rpm with v fixed at 10 mV s^{-1}, and the corresponding J_L was quantified as 4.02, 4.87, 5.98, 7.12, and 8.26 mA cm^{-2}, respectively (Figure 2A). The slope A in Equation 2 is fitted as 1.67 mA^{-1} cm^2 s$^{-1/2}$ (Figure 2B). For the CV tests, the v was 10, 20, 50, 100, or 200 mV s^{-1} without RDE rotation (Figure 2C). The corresponding J_P was quantified as 0.978, 1.34, 2.06, 2.86, and 3.98 mA cm^{-2}, and the slope B is calculated as 8.64 mA cm^{-2} V$^{-1/2}$ s$^{1/2}$ (Figure 2D). Combining Equations 2 and 4, the n and D values are solved as 1.43 and 5.17×10^{-6} cm^2 s^{-1}, respectively (Figure 2E).

Analogous to the 20% HME system, the n and D values in other systems of 0%, 10%, 30%, 40%, and 50% HME can be obtained (Figures S7–S31). With the increase of the HME content, the n of Li_2S_8 oxidation gradually reduces from 1.68 to 1.10 (Figure S32). The lowered n indicates that the LiPS oxidation extent is intrinsically suppressed as the electrolyte solvating power is weakened, fundamentally manifesting the impaired LiPS kinetics in WSEs.

Reduced hydrodynamic radius reveals anti-aggregation effect

Interestingly, the D and μ values increase simultaneously as the HME content rises. Concretely, the D increases from 3.70 × 10^{-6} to 7.91 × 10^{-6} cm^2 s^{-1} when the HME content changes from 0% to 50% (Figure 3A). To understand the above tendency at the molecular level, the LiPS hydrodynamic radius (r) in

Please cite this article in press as: Jin et al., Reducing polysulfide hydrodynamic radius toward low-temperature lithium–sulfur batteries, Chem (2025), https://doi.org/10.1016/j.chempr.2025.102881

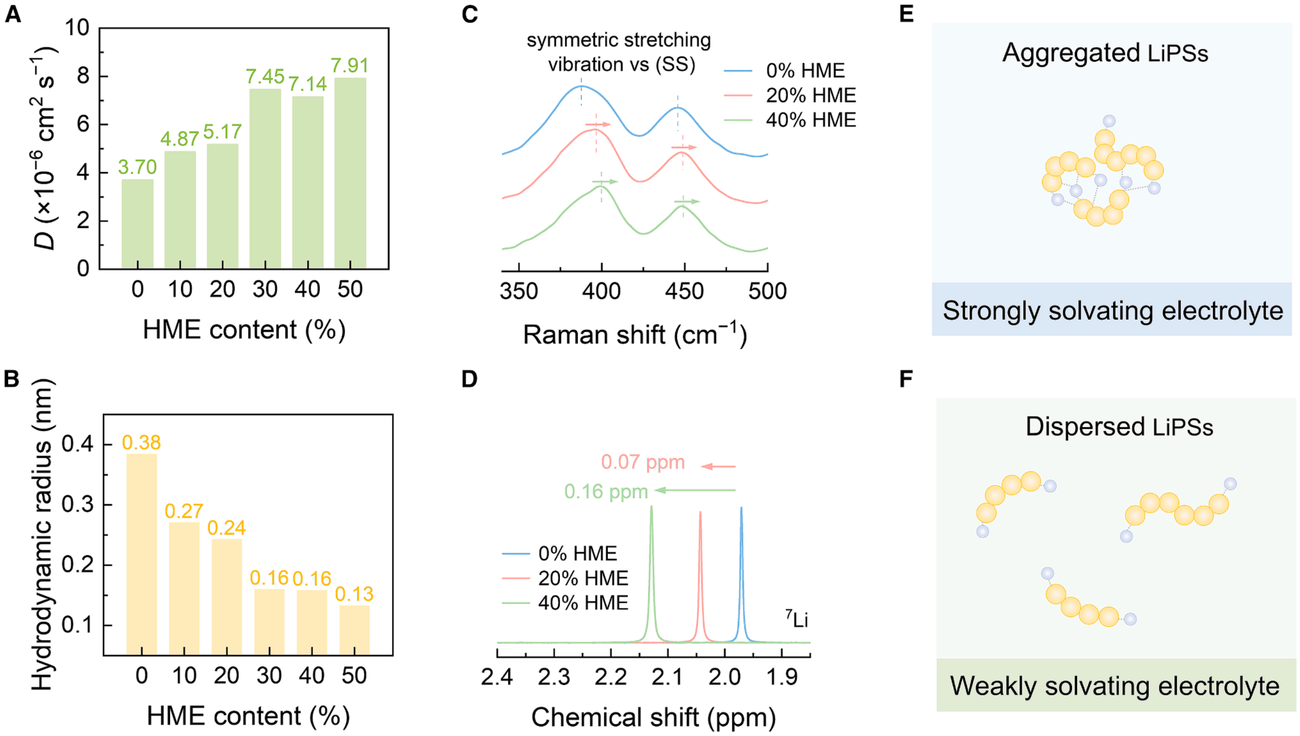

Figure 3. LiPS aggregation in WSEs with variable HME contents

(A) The measured diffusion coefficients of Li_2S_8.

(B) Calculated hydrodynamic radius.

(C and D) (C) Raman spectra and (D) ^{7}Li-NMR spectra of LiPSs.

(E and F) Aggregation schematics of LiPSs in strongly solvating electrolyte and WSE.

WSEs is ascertained through the Stokes–Einstein equation as follows:[23]

$$r = \frac{k_B T}{6\pi\mu D} \qquad \text{(Equation 5)}$$

where k_B is Boltzmann's constant (1.38065×10^{-23} J K^{-1}). A progressive reduction of r is observed with the rise of the HME content. In detail, the r decreases from 0.38 to 0.13 nm when the HME content varies from 0% to 50%, corresponding to a 65.8% contraction (Figure 3B). The lowered r suggests that the aggregation tendency of LiPSs in WSEs is inhibited, accounting for the diffusion coefficient increase.

To verify the inhibited aggregation of LiPSs in WSEs, spectroscopic analyses with variable HME contents were further conducted. As the HME content increases, the Raman shift of the S–S symmetric vibration mode is upshifted from 387 to 400 cm^{-1} (Figure 3C),[24] indicating the S–S bond in LiPSs is less restrained, and the aggregation degree of LiPSs is lower in WSEs.[25] The chemical environment of lithium in LiPSs was also probed. According to the ^{7}Li-nuclear magnetic resonance (NMR) spectrum, the peak chemical shift moves from 1.97 to 2.13 ppm as the HME content increases (Figure 3D). The low-field shift indicates the electron density around lithium is decreased, suggesting the interaction between the polysulfide chain and lithium is weakened and the LiPS aggregation degree is reduced in WSEs. Based on the Raman and NMR analysis, WSEs can regulate the LiPS solvation structure and reduce the intermolecular aggregation of LiPSs (Figures 3E and 3F).

Anti-aggregation enables exceptional low-temperature performance

Previous research by Manthiram et al. indicated that the LiPS kinetics was constrained by the advent of LiPS aggregation, particularly at low-temperature conditions.[26,27] Our study confirms WSEs can inhibit LiPS aggregation, suggesting Li–S batteries with WSEs are endowed with better low-temperature performances. To this end, coin cells with sulfur loadings of 4.0 mg_S cm^{-2} were assembled and tested at −20°C using 20% HME (denoted as WSE) or conventional electrolyte (denoted as DOL/DME). Under low rates of 0.01 and 0.02 C (1 C = 1,672 mA g^{-1}), the cells with WSE provide similar specific discharge capacity as DOL/DME, while the discharge polarization is lower in WSE to indicate improved kinetics (Figures S33 and S34). Under higher rates of 0.025, 0.03, and 0.04 C, the cells with WSE can still deliver specific discharge capacities of 853, 813, and 771 mAh g^{-1}, respectively, while those in batteries with DOL/DME are smaller than 250 mAh g^{-1} due to the large polarization at the second discharge plateau (Figures 4A, S35, and S36). Notably, the cells with WSE achieve 759 mAh g^{-1} at 0.05 C, while the cells with DOL/DME can hardly discharge (Figure S37). Obviously, Li–S batteries with WSEs have better rate performances at low temperatures (Figure S38). In addition, the cells with WSE

Please cite this article in press as: Jin et al., Reducing polysulfide hydrodynamic radius toward low-temperature lithium–sulfur batteries, Chem (2025), https://doi.org/10.1016/j.chempr.2025.102881

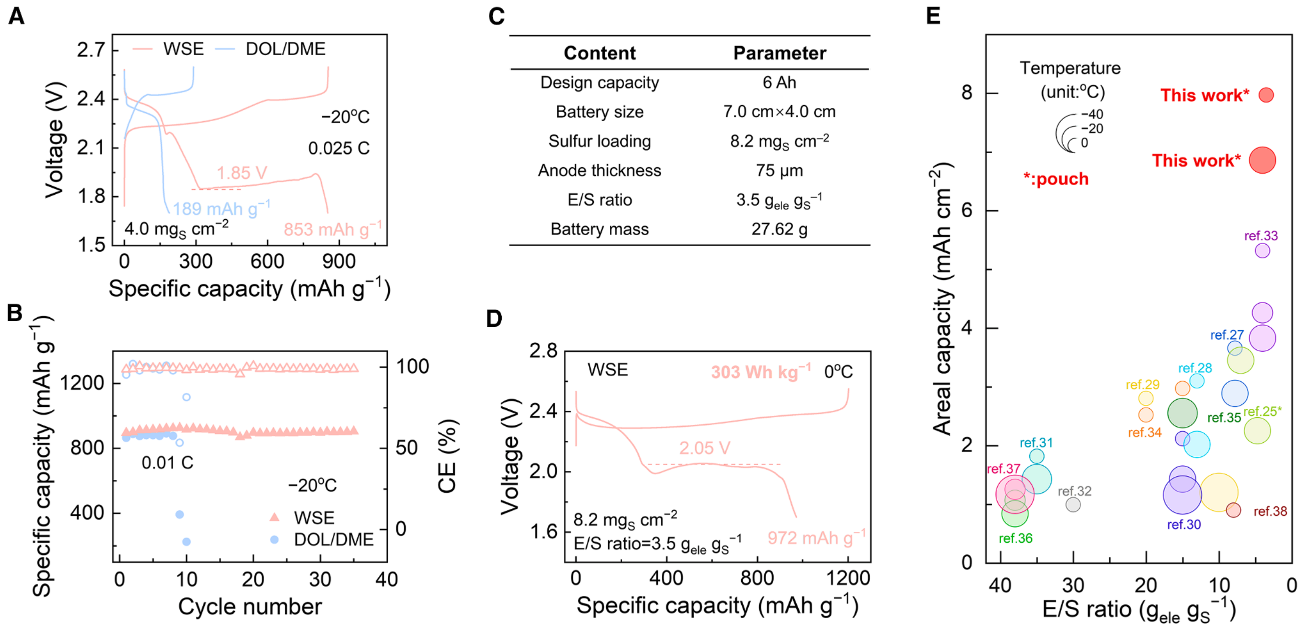

Content	Parameter
Design capacity	6 Ah
Battery size	7.0 cm×4.0 cm
Sulfur loading	8.2 mg$_S$ cm^{-2}
Anode thickness	75 μm
E/S ratio	3.5 g$_{ele}$ g$_S$$^{-1}$
Battery mass	27.62 g

Figure 4. Low-temperature performances of Li–S batteries with WSEs

(A) Charge-discharge profiles of Li–S coin cells with WSE or DOL/DME at −20°C.

(B) Cycling performance of Li–S coin cells with WSE or DOL/DME at −20°C.

(C and D) (C) Design parameters and (D) charge-discharge profile of 6 Ah-level Li–S pouch cell with WSE at 0°C.

(E) Low-temperature battery performance comparison.

operate stably for over 35 cycles at 0.01 C at −20°C, while the cells with DOL/DME fail after 8 cycles due to the large polarization at the second discharge plateau (Figure 4B).

To further verify the low-temperature advantage of WSEs in practical Li–S batteries, 6 Ah-level pouch cells were assembled and tested. The pouch cells featured high-sulfur-loading cathodes of 8.2 mg$_S$ cm^{-2}, ultrathin lithium anodes of 75 μm in thickness, and a very low electrolyte-to-sulfur (E/S) ratio of 3.5 g$_{ele}$ g$_S$$^{-1}$ (Figures 4C and S39). The pouch cell delivers 1,293 mAh g^{-1} and an actual energy density of 410 Wh kg^{-1} at 25°C based on the total mass (Figure S40). At 0°C, the pouch cell also maintains 972 mAh g^{-1} and an areal capacity of 8.0 mAh cm^{-2}, achieving an actual energy density of 303 Wh kg^{-1} that preserves 75% of its value at 25°C with stable cycling ability (Figures 4D and S41). Moreover, the WSE-based pouch cell outperforms the one with DOL/DME electrolyte in the initial specific discharge capacity (Figure S42). Another pouch cell was tested at −20°C under an E/S ratio of 4.0 g$_{ele}$ g$_S$$^{-1}$, achieving a specific discharge capacity of 847 mAh g^{-1} and an areal capacity of 6.9 mAh cm^{-2} (Figures S43 and S44; Table S1). The pouch cell performances have exceeded previous Li–S reports in realizing high areal capacity under low-temperature and lean-electrolyte conditions (Figure 4E; Table S2).[25,27–38] To sum up, the aggregation tendency of LiPSs is inhibited in WSEs so that the low-temperature performances of Li–S batteries are unexpectedly promoted using WSEs.

In summary, a quantitative analytical method based on RDE is established to evaluate the intrinsic LiPS kinetics in WSEs. As the HME content increases, the electron transfer number is reduced by 34.5% during LiPS oxidation to indicate the suppressed reaction extent. Stokes–Einstein analysis confirms a 65.8% reduction in hydrodynamic radius, corresponding to the suppression of LiPS aggregation in WSEs. This unique anti-aggregation characteristic endows Li–S batteries with exceptional low-temperature performances with a specific discharge capacity of 853 mAh g^{-1} at −20°C and 303 Wh kg^{-1} at 0°C in 6 Ah-level pouch cells. This work presents a new kinetic analysis framework to guide rational electrolyte design and underscores the potential of WSE-based Li–S batteries for low-temperature applications.

METHODS

Raw materials

All the raw materials, including 1,3-dioxolane (DOL), 1,2-dimethoxyethane (DME), HME, sulfur (S_8), lithium sulfide (Li_2S), lithium nitrate ($LiNO_3$), lithium bis(trifluoromethanesulfonyl)imide (LiTFSI), deuterated chloroform ($CDCl_3$), carbon nanotubes (CNTs), poly(vinylidenefluoride) (PVDF), N-methyl pyrrolidone (NMP), polypropylene (PP) separator (Celgard 2500), aluminum (Al) foil, copper (Cu) foil, and lithium (Li) foil, were purchased from commercial sources and directly used without further purification.

Preparation of electrolyte

HME solvent was mixed with DOL/DME (v/v = 1:3) solvents with volume ratios of 0%, 10%, 20%, 30%, 40%, or 50% and denoted as the HME/DOL/DME mixed solvents. Then, 1.0 mol L^{-1} LiTFSI was dissolved in the above HME/DOL/DME mixed solvents and was denoted as 0% HME, 10% HME, 20% HME, 30% HME, 40% HME, and 50% HME electrolyte, respectively.

Please cite this article in press as: Jin et al., Reducing polysulfide hydrodynamic radius toward low-temperature lithium–sulfur batteries, Chem (2025), https://doi.org/10.1016/j.chempr.2025.102881

To prepare the Li_2S_8 electrolytes, Li_2S and S_8 were mixed in the above HME electrolytes with a molar ratio of 8:7 and stirred at 55°C until full dissolution. To facilitate experimental consistency, the Li_2S_8 concentration was first set as 100 $\mathrm{mmol_S}$ in 1,000 mL HME electrolytes with varied HME contents and then calibrated according to the density of the electrolyte for the RDE analysis in the three-electrode system, and the calibrated concentrations are exhibited in Figure S4. As for Raman and NMR spectra measurements, the Li_2S_8 concentration was controlled as 1.0 $\mathrm{mol_S\ L^{-1}}$ nominally in HME electrolytes.

For the coin cell tests in Figure 4, the electrolyte consisting of 1.0 mol L^{-1} LiTFSI and 2.0 wt % $LiNO_3$ in DOL/DME (1:3, by vol.) was designated as DOL/DME. The electrolyte comprising of 1.0 mol L^{-1} LiTFSI and 2.0 wt % $LiNO_3$ in DOL/DME/HME (1:3:1, by vol.) was designated as WSE.

For the pouch cell test in Figure 4, the electrolyte containing 0.60 mol L^{-1} LiTFSI and 5.0 wt % $LiNO_3$ in DOL/DME/HME (1:3:1, by vol.) was designated as WSE.

RDE tests

A Ag/AgCl electrode was used as the reference electrode, a Li foil served as the counter electrode, and a RDE equipped with a glassy carbon disk with a diameter of 5.0 mm (Pine Research Instrument, USA) served as the working electrode.

12 mL Li_2S_8 electrolytes with variable HME contents were employed as the electrolytes. For the LSV tests, the scan rate was fixed at 10 mV s^{-1} within a voltage range from the open-circuit potential to 0.2 V (versus Ag/AgCl), and the rotating rates were controlled as 400, 625, 900, 1,225, or 1,600 rpm, corresponding to rotating speeds (ω) of 41.9, 65.5, 94.3, 128, and 168 rad s^{-1}, respectively. For the CV tests, the measurements were conducted at scan rates of 10, 20, 50, 100, or 200 mV s^{-1} within a voltage range from the open-circuit potential to 0.2 V (versus Ag/AgCl) without RDE rotation.

For the electrolyte physical property measurements, as previously mentioned, the actual concentration of Li_2S_8 in the electrolyte needs to be corrected due to the volume expansion effect caused by the varying HME content. To achieve this, the density ρ of the Li_2S_8 electrolytes was determined by measuring the mass of a fixed volume of electrolyte using an analytical balance (Mettler Toledo, Switzerland). Based on the measured density and the known electrolyte mass, the actual volume of the Li_2S_8 electrolyte was calculated, allowing for the determination of the corrected molecular concentration of Li_2S_8 under different HME content conditions, as shown in Figures S3 and S4. The dynamic viscosities (μ) of electrolytes can be measured using a viscometer (LC-DV-LV, China). The kinematic viscosity (υ) was further obtained by dividing the dynamic viscosity μ by the electrolyte density ρ, according to the following equation:

$$\upsilon = \frac{\mu}{\rho}$$

Spectroscopic characterizations

For the Raman spectroscopy measurements, 0% HME, 20% HME, and 40% HME electrolytes containing 1.0 $\mathrm{mol_S\ L^{-1}}$ Li_2S_8 were filled into quartz glass cuvettes, and the spectra were acquired using a Horiba Jobin Yvon LabRAM HR800 Raman spectrometer equipped with a 532 nm He-Ne laser.

For the NMR analyses, ^{7}Li-NMR spectra were recorded using a JNM-ECZ400 NMR spectrometer to detect the Li_2S_8 surrounding environments in electrolytes. In detail, coaxial NMR tubes were employed, with pure $CDCl_3$ solvents (as the deuterated reagent) loaded in the inner tube for field locking, while the outer tube was filled with 0% HME, 20% HME, and 40% HME electrolyte containing 1.0 $\mathrm{mol_S\ L^{-1}}$ Li_2S_8, respectively.

Cathode preparation

Sulfur and CNTs were mixed in a batch with a mass ratio of 7:3. The mixture was then ball-milled with PVDF binder in NMP at a weight ratio of 9:1 to form a slurry. The obtained slurry was then coated on one or both sides of Al foils and fully dried at 60°C for 24 h to prepare sulfur/carbon (S/C) cathodes for assembly of coin or pouch cells. The sulfur content in the S/C cathode was 63 wt.%. For the coin cells, the areal sulfur loading was controlled as 4.0 $\mathrm{mg_S\ cm^{-2}}$, and the cathode was cut into disks with a diameter of 13.0 mm. For the 6 Ah-level pouch cells, the areal sulfur loading was ~8.2 $\mathrm{mg_S\ cm^{-2}}$ on a single side, and the S/C cathodes were cut into 7.0 × 4.0 cm^2 square pieces.

Electrochemical measurements

Electrochemical tests on Li–S coin cells

Li–S coin cells were assembled using standard 2032-coin cell configurations comprising a 600 μm-thick Li anode (16.0 mm in diameter), a PP separator (19.0 mm in diameter), and the S/C cathode (13.0 mm in diameter) with areal sulfur loading of 4.0 $\mathrm{mg_S\ cm^{-2}}$. Each cell was injected with 55 μL electrolyte.

Firstly, all the tested cells were activated at 0.05 C (1 C = 1,672 mA g^{-1}) between 1.70–2.60 V on a LAND multichannel battery cycler at 25°C. In the low-temperature test, for the rate tests, the cells were galvanostatically cycled at 0.01, 0.02, 0.025, 0.03, 0.04, and 0.05 C between 1.70 and 2.60 V on a LAND multichannel battery cycler at −20°C. For the cycling tests, the cells were cycled galvanostatically at 0.01 C between 1.70 and 2.60 V on the LAND multichannel battery cycler at −20°C.

Electrochemical tests on Li–S pouch cells

Li-S pouch cells were fabricated in a dry room (dew point < −40°C). The anode of the Li–S pouch cells was double-sided Li metal rolled on Cu current collectors with a size of 4.0 × 7.0 cm^2 (75 μm thickness on a single side). For the 6 Ah-level Li–S pouch cells, the areal sulfur loading was ~8.2 $\mathrm{mg_S\ cm^{-2}}$ on a single side. For the assembly of the Li–S pouch cells, the cathodes, separators, and anodes were stacked layer by layer. The electrodes were controlled in parallel connection by using an electrode lug terminal.

Firstly, all the tested cells were activated at 0.025 C (1 C = 1,000 mA g^{-1}) between 1.70 and 2.55 V on a LAND multichannel battery cycler at 25°C. The low-temperature test of the pouch cells was carried out at 0°C or −20°C. For the cells tested at 0°C, the E/S ratio was 3.5 $\mathrm{g_{ele}\ g_S{}^{-1}}$, and the cells were galvanostatically cycled at 0.01 C between 1.70 and 2.55 V on the NEWARE battery cycler. For the cells tested at −20°C, the E/S ratio was 4.0 $\mathrm{g_{ele}\ g_S{}^{-1}}$, and the cells were galvanostatically cycled at 0.005 C between 1.50 and 2.55 V on the NEWARE battery cycler.

RESOURCE AVAILABILITY

Lead contact

Requests for further information and resources should be directed to and will be fulfilled by the lead contact, Qiang Zhang (zhang-qiang@mails.tsinghua.edu.cn).

Materials availability

All reagents used in this work are commercially available or can be prepared according to the procedures described above.

Data and code availability

The data supporting this study are available in the manuscript and supplemental information. Additional information is available from the lead contact upon reasonable request.

ACKNOWLEDGMENTS

This work was supported by the National Key Research and Development Program of China (2024YFE0209500), the Beijing Municipal Natural Science Foundation (L233004), and the National Natural Science Foundation of China (22425901, 22409116, 224B2913, and 22393900). The authors thank Y.-C.G. and Z.-Y.S. for helpful discussion.

AUTHOR CONTRIBUTIONS

Conceptualization, Q.Z. and M.Z.; methodology, T.J., B.-Q.L., and M.Z.; investigation, T.J., X.-Y.L., and Z.-X.C.; writing—original draft, T.J.; writing—review & editing, T.J., Z.-X.C., M.Z., B.-Q.L., J.-Q.H., and Q.Z.; funding acquisition, Q.Z. and M.Z.; resources, Q.Z. and M.Z.; supervision, Q.Z. and M.Z.

DECLARATION OF INTERESTS

The authors declare no competing interests.

SUPPLEMENTAL INFORMATION

Supplemental information can be found online at https://doi.org/10.1016/j.chempr.2025.102881.

Received: August 19, 2025
Revised: November 14, 2025
Accepted: December 1, 2025

REFERENCES

1. Yao, N., Chen, X., Sun, S.-Y., Gao, Y.-C., Yu, L., Gao, Y.-B., Li, W.-L., and Zhang, Q. (2025). Identifying the lithium bond and lithium ionic bond in electrolytes. Chem *11*, 102254. https://doi.org/10.1016/j.chempr.2024.07.016.
2. Song, H., Münch, K., Liu, X., Shen, K., Zhang, R., Weintraut, T., Yusim, Y., Jiang, D., Hong, X., Meng, J., et al. (2025). All-solid-state Li–S batteries with fast solid–solid sulfur reaction. Nature *637*, 846–853. https://doi.org/10.1038/s41586-024-08298-9.
3. Liu, Y., An, Y., Fang, C., Ye, Y., An, Y., He, M., Jia, Y., Hong, X., Liu, Y., Gao, S., et al. (2025). Surface-localized phase mediation accelerates quasi-solid-state reaction kinetics in sulfur batteries. Nat. Chem. *17*, 614–623. https://doi.org/10.1038/s41557-025-01735-w.
4. Song, Y.-W., Shen, L., Li, X.-Y., Zhao, C.-X., Zhou, J., Li, B.-Q., Huang, J.-Q., and Zhang, Q. (2024). Phase equilibrium thermodynamics of l ithium–sulfur batteries. Nat. Chem. Eng. *1*, 588–596. https://doi.org/10.1038/s44286-024-00115-4.
5. Zhang, Y., Yu, T., Xiao, R., Tang, P., Fang, R., Li, Z., Cheng, H.M., Sun, Z., and Li, F. (2025). The role of long-range interactions between high-entropy single-atoms in catalyzing sulfur conversion reactions. Adv. Mater. *37*, 2413653. https://doi.org/10.1002/adma.202413653.
6. Chen, J., Lu, H., Kong, X., Liu, J., Liu, J., Yang, J., Nuli, Y., and Wang, J. (2024). Interphase engineering via solvent molecule chemistry for stable lithium metal batteries. Angew. Chem. Int. Ed. *63*, e202317923. https://doi.org/10.1002/anie.202317923.
7. Cheng, Q., Chen, Z.-X., Li, X.-Y., Hou, L.-P., Bi, C.-X., Zhang, X.-Q., Huang, J.-Q., and Li, B.-Q. (2023). Constructing a 700 Wh kg^{-1}-level rechargeable lithium–sulfur pouch cell. J. Energy Chem. *76*, 181–186. https://doi.org/10.1016/j.jechem.2022.09.029.
8. Hou, T.Z., Xu, W.T., Chen, X., Peng, H.J., Huang, J.Q., and Zhang, Q. (2017). Lithium bond chemistry in lithium–sulfur batteries. Angew. Chem. Int. Ed. *56*, 8178–8182. https://doi.org/10.1002/anie.201704324.
9. Bi, C.X., Yao, N., Li, X.Y., Zhang, Q.K., Chen, X., Zhang, X.Q., Li, B.Q., and Huang, J.Q. (2024). Unveiling the reaction mystery between lithium polysulfides and lithium metal anode in lithium–sulfur batteries. Adv. Mater. *36*, 2411197. https://doi.org/10.1002/adma.202411197.
10. Kwok, C.Y., Xu, S., Kochetkov, I., Zhou, L., and Nazar, L.F. (2023). High-performance all-solid-state Li_2S batteries using an interfacial redox mediator. Energy Environ. Sci. *16*, 610–618. https://doi.org/10.1039/D2EE03297J.
11. Suo, L., Hu, Y.-S., Li, H., Armand, M., and Chen, L. (2013). A new class of solvent-in-salt electrolyte for high-energy rechargeable metallic lithium batteries. Nat. Commun. *4*, 1481. https://doi.org/10.1038/ncomms2513.
12. Ma, T., Ni, Y., Li, D., Zha, Z., Jin, S., Zhang, W., Jia, L., Sun, Q., Xie, W., Tao, Z., et al. (2023). Reversible solid–solid conversion of sulfurized polyacrylonitrile cathodes in lithium–sulfur batteries by weakly solvating ether electrolytes. Angew. Chem. Int. Ed. *62*, e202310761. https://doi.org/10.1002/anie.202310761.
13. Hou, L.-P., Zhang, X.-Q., Yao, N., Chen, X., Li, B.-Q., Shi, P., Jin, C.-B., Huang, J.-Q., and Zhang, Q. (2022). An encapsulating lithium-polysulfide electrolyte for practical lithium–sulfur batteries. Chem *8*, 1083–1098. https://doi.org/10.1016/j.chempr.2021.12.023.
14. Su, L.L., Yao, N., Li, Z., Bi, C.X., Chen, Z.X., Chen, X., Li, B.Q., Zhang, X.Q., and Huang, J.Q. (2024). Improving rate performance of encapsulating lithium-polysulfide electrolytes for practical lithium−sulfur batteries. Angew. Chem. Int. Ed. *63*, e202318785. https://doi.org/10.1002/anie.202318785.
15. Liu, Y., Xu, L., Yu, Y., He, M., Zhang, H., Tang, Y., Xiong, F., Gao, S., Li, A., Wang, J., et al. (2023). Stabilized Li–S batteries with anti-solvent-tamed quasi-solid-state reaction. Joule *7*, 2074–2091. https://doi.org/10.1016/j.joule.2023.07.013.
16. Liu, T., Li, H., Yue, J., Feng, J., Mao, M., Zhu, X., Hu, Y.-S., Li, H., Huang, X., Chen, L., et al. (2021). Ultralight electrolyte for high-energy lithium–sulfur pouch cells. Angew. Chem. Int. Ed. *60*, 17547–17555. https://doi.org/10.1002/anie.202103303.
17. Lee, C.-W., Pang, Q., Ha, S., Cheng, L., Han, S.-D., Zavadil, K.R., Gallagher, K.G., Nazar, L.F., and Balasubramanian, M. (2017). Directing the lithium–sulfur reaction pathway via sparingly solvating electrolytes for high energy density batteries. ACS Cent. Sci. *3*, 605–613. https://doi.org/10.1021/acscentsci.7b00123.
18. Li, Z., Hou, L.P., Yao, N., Li, X.Y., Chen, Z.X., Chen, X., Zhang, X.Q., Li, B.Q., and Zhang, Q. (2023). Correlating polysulfide solvation structure with electrode kinetics towards long-cycling lithium–sulfur batteries. Angew. Chem. Int. Ed. *62*, e202309968. https://doi.org/10.1002/anie.202309968.
19. Li, X.-Y., Feng, S., Song, Y.-W., Zhao, C.-X., Li, Z., Chen, Z.-X., Cheng, Q., Chen, X., Zhang, X.-Q., Li, B.-Q., et al. (2024). Kinetic evaluation on lithium polysulfide in weakly solvating electrolyte toward practical lithium–sulfur batteries. J. Am. Chem. Soc. *146*, 14754–14764. https://doi.org/10.1021/jacs.4c02603.
20. Lazaridis, T., Stühmeier, B.M., Gasteiger, H.A., and El-Sayed, H.A. (2022). Capabilities and limitations of rotating disk electrodes versus membrane

Please cite this article in press as: Jin et al., Reducing polysulfide hydrodynamic radius toward low-temperature lithium–sulfur batteries, Chem (2025), https://doi.org/10.1016/j.chempr.2025.102881

electrode assemblies in the investigation of electrocatalysts. Nat. Catal. *5*, 363–373. https://doi.org/10.1038/s41929-022-00776-5.

21. Zhou, R., Zheng, Y., Jaroniec, M., and Qiao, S.-Z. (2016). Determination of the electron transfer number for the oxygen reduction reaction: From theory to experiment. ACS Catal. *6*, 4720–4728. https://doi.org/10.1021/acscatal.6b01581.
22. Yu, D.Y.W., Fietzek, C., Weydanz, W., Donoue, K., Inoue, T., Kurokawa, H., and Fujitani, S. (2007). Study of $LiFePO_4$ by cyclic voltammetry. J. Electrochem. Soc. *154*, A253. https://doi.org/10.1149/1.2434687.
23. Nordness, O., and Brennecke, J.F. (2020). Ion dissociation in ionic liquids and ionic liquid solutions. Chem. Rev. *120*, 12873–12902. https://doi.org/10.1021/acs.chemrev.0c00373.
24. Liu, R., Wei, Z., Peng, L., Zhang, L., Zohar, A., Schoeppner, R., Wang, P., Wan, C., Zhu, D., Liu, H., et al. (2024). Establishing reaction networks in the 16-electron sulfur reduction reaction. Nature *626*, 98–104. https://doi.org/10.1038/s41586-023-06918-4.
25. Kim, S., Jung, J., Kim, I., Kwon, H., Cho, H., and Kim, H.T. (2023). Tuning of electrolyte solvation structure for low-temperature operation of lithium–sulfur batteries. Energy Storage Mater. *59*, 102763. https://doi.org/10.1016/j.ensm.2023.04.002.
26. Gupta, A., and Manthiram, A. (2021). Unifying the clustering kinetics of lithium polysulfides with the nucleation behavior of Li_2S in lithium–sulfur batteries. J. Mater. Chem. A *9*, 13242–13251. https://doi.org/10.1039/D1TA02779D.
27. Gupta, A., Bhargav, A., Jones, J.-P., Bugga, R.V., and Manthiram, A. (2020). Influence of lithium polysulfide clustering on the kinetics of electrochemical conversion in lithium–sulfur batteries. Chem. Mater. *32*, 2070–2077. https://doi.org/10.1021/acs.chemmater.9b05164.
28. Gupta, A., Bhargav, A., and Manthiram, A. (2021). Tailoring lithium polysulfide coordination and clustering behavior through cationic electrostatic competition. Chem. Mater. *33*, 3457–3466. https://doi.org/10.1021/acs.chemmater.1c00893.
29. Wang, Z., Ji, H., Zhou, L., Shen, X., Gao, L., Liu, J., Yang, T., Qian, T., and Yan, C. (2021). All-liquid-phase reaction mechanism enabling cryogenic Li–S batteries. ACS Nano *15*, 13847–13856. https://doi.org/10.1021/acsnano.1c05875.
30. Deng, D.R., Xue, F., Bai, C.-D., Lei, J., Yuan, R., Zheng, M.S., and Dong, Q.F. (2018). Enhanced adsorptions to polysulfides on graphene-supported BN nanosheets with excellent Li–S battery performance in a wide temperature range. ACS Nano *12*, 11120–11129. https://doi.org/10.1021/acsnano.8b05534.
31. Fan, C.-Y., Zheng, Y.-P., Zhang, X.-H., Shi, Y.-H., Liu, S.-Y., Wang, H.-C., Wu, X.-L., Sun, H.-Z., and Zhang, J.-P. (2018). High-performance and low-temperature lithium–sulfur batteries: Synergism of thermodynamic and kinetic regulation. Adv. Energy Mater. *8*, 1703638. https://doi.org/10.1002/aenm.201703638.
32. Na, F., Li, X., Wang, J., Cheng, X., Zhang, J., Wang, Y., Lin, H., Zhan, L., Ling, L., and Zhang, Y. (2025). Immobilizing single atom on high-entropy oxides as separator regulators for catalyzing low-temperature lithium–sulfur battery. Energy Storage Mater. *78*, 104228. https://doi.org/10.1016/j.ensm.2025.104228.
33. Ji, H., Chen, X., Cheng, Z., Yuan, L., Miao, Z., Xiang, J., Zhang, Y., He, B., Meng, J., Li, Z., et al. (2022). Improved low-temperature performance of Li–S batteries via "solid-solid" conversion of sulfur. J. Electrochem. Soc. *169*, 100529. https://doi.org/10.1149/1945-7111/ac992d.
34. Chu, F., Wang, M., Liu, J., Guan, Z., Yu, H., Liu, B., and Wu, F. (2022). Low concentration electrolyte enabling cryogenic lithium–sulfur batteries. Adv. Funct. Mater. *32*, 2205393. https://doi.org/10.1002/adfm.202205393.
35. Wang, Y., Xu, Y., Ma, S., Duan, R., Zhao, Y., Zhang, Y., Liu, Z., and Li, C. (2020). Low temperature performance enhancement of high-safety lithium–sulfur battery enabled by synergetic adsorption and catalysis. Electrochim. Acta *353*, 136470. https://doi.org/10.1016/j.electacta.2020.136470.
36. Gao, N., Zhang, Y., Chen, C., Li, B., Li, W., Lu, H., Yu, L., Zheng, S., and Wang, B. (2022). Low-temperature Li–S battery enabled by CoFe bimetallic catalysts. J. Mater. Chem. A *10*, 8378–8389. https://doi.org/10.1039/D2TA00406B.
37. Pang, X., An, B., Zheng, S., and Wang, B. (2023). Synergistic enhancement of Li–S battery low-temperature cycling performance by nano-sized uniformly compounded FeCoNi and MnO nanoparticles. Chem. Eng. J. *458*, 141445. https://doi.org/10.1016/j.cej.2023.141445.
38. Ma, Z., Liu, W., Jiang, X., Liu, Y., Yang, G., Wu, Z., Zhou, Q., Chen, M., Xie, J., Ni, L., et al. (2022). Wide-temperature-range Li–S batteries enabled by thiodimolybdate $[Mo_2S_{12}]^{2-}$ as a dual-function molecular catalyst for polysulfide redox and lithium intercalation. ACS Nano *16*, 14569–14581. https://doi.org/10.1021/acsnano.2c05029.